*J. Fluid Mech.* (2024), *vol*. 995, R4, doi:10.1017/jfm.2024.785

# Instabilities and particle-induced patterns in co-rotating suspension Taylor–Couette flow

**Manojit Ghosh**[1] **and Meheboob Alam**[1],†

[1]Engineering Mechanics Unit, Jawaharlal Nehru Centre for Advanced Scientific Research, Jakkur P.O., Bangalore 560064, India

(Received 10 May 2024; revised 26 June 2024; accepted 28 June 2024)

The first experimental results on pattern transitions in the co-rotation regime (i.e. the rotation ratio $\Omega = \omega_o/\omega_i > 0$, where $\omega_i$ and $\omega_o$ are the angular speeds of the inner and outer cylinders, respectively) of the Taylor–Couette flow (TCF) are reported for a neutrally buoyant suspension of non-colloidal particles, up to a particle volume fraction of $\phi = 0.3$. While the stationary Taylor vortex flow (TVF) is the primary bifurcating state in dilute suspensions ($\phi \leq 0.05$), the non-axisymmetric oscillatory states, such as the spiral vortex flow (SVF) and the ribbon (RIB), appear as primary bifurcations with increasing particle loading, with an overall de-stabilization of the primary bifurcating states (TVF/SVF/RIB) being found with increasing $\phi$ for all $\Omega \geq 0$. At small co-rotations ($\Omega \sim 0$), the particles play the dual role of stabilization ($\phi < 0.1$) and destabilization ($\phi \geq 0.1$) on the secondary/tertiary oscillatory states. The distinctive features of the 'particle-induced' spiral vortices are identified and contrasted with those of the 'fluid-induced' spirals that operate in the counter-rotation regime.

**Key words:** suspensions, Taylor–Couette flow, pattern formation

## 1. Introduction

The fluid flow between two independently rotating co-axial cylinders (Couette 1888; Taylor 1923), known as the Taylor–Couette flow (TCF), has served as a canonical set-up to study instabilities and pattern transitions, leading to chaos and turbulence, over the past century (Rayleigh 1917; Synge 1938; Coles 1965; Gollub & Swinney 1975; Mullin & Benjamin 1980; Andereck, Liu & Swinney 1986; Dutcher & Muller 2009; Grossmann, Lohse & Sun 2016; Lueptow, Hollerbach & Serre 2023). Adding neutrally buoyant, non-colloidal rigid particles to Newtonian fluids can significantly alter the flow transitions in the TCF as revealed in recent experiments (Majji, Banerjee & Morris 2018; Ramesh, Bharadwaj & Alam 2019; Baroudi, Majji & Morris 2020; Dash,

† Email address for correspondence: meheboob@jncasr.ac.in

Anantharaman & Poelma 2020; Ramesh & Alam 2020; Moazzen *et al.* 2022). The first comprehensive experimental investigation of suspension TCF was conducted by Majji *et al.* (2018) for the case of pure inner cylinder rotation ($\Omega = \omega_0/\omega_i = 0$), which showed that the critical Reynolds number for the primary bifurcation $Re^{c1}(\phi, \Omega = 0)$ decreases with increasing particle volume fraction $\phi$, implying the destabilizing role of particles. They discovered 'particle-induced' non-axisymmetric patterns, namely, the spiral vortex flow (SVF) and/or ribbon (RIB), that appear as the primary bifurcating state when the particle loading exceeds a critical value $\phi^{cr} \sim 0.05$. Ramesh *et al.* (2019) conducted flow visualization and particle image velocimetry measurements, and identified two co-existing/mixed states: (i) Taylor vortex flow (TVF)+wavy Taylor vortex (WTV) and (ii) TVF+SVF, during the up-sweep run for $\phi \geq 0.05$; however, a transition sequence of CCF $\leftarrow$ SVF $\leftarrow$ TVF $\leftarrow$ WTV was found during the down-sweep run. The later work of Ramesh & Alam (2020) uncovered another state of interpenetrating spiral vortices (ISVs), i.e. the coexistence of up- and down-propagating spiral vortices, which appears as a secondary bifurcation from the mixed 'TVF+SVF' state for $\phi \geq 0.1$. Baroudi *et al.* (2020) explored the effect of inertial migration (due to finite values of the particle Reynolds number) on observed patterns in TCF. Dash *et al.* (2020) carried out experiments over a large range of Reynolds number ($Re \sim O(10^3)$) and explored higher order transitions for $\phi \leq 0.4$; they identified a power-law scaling for the normalized torque that holds beyond the secondary bifurcation. Moazzen *et al.* (2022) carried out torque measurement and flow visualization in an identical experimental set-up as used by Ramesh *et al.* (2019) and determined the scaling exponents of the normalized torque in terms of Taylor number in the TVF and WTV regimes. The earliest theoretical work on suspension TCF is due to Ali *et al.* (2002), who analysed the linear stability problem for a 'dilute' suspension ($\phi < 0.05$) based on a two-fluid model, and predicted the destabilizing role of particles at the onset of primary instability. Most recently, Kang & Mirbod (Kang & Mirbod 2021; Kang, Schatz & Mirbod 2024) performed numerical simulations to study pattern transitions in suspension TCF using the suspension balance model and found a qualitative agreement (Baroudi *et al.* 2023) with recent experimental findings.

Considering two independently rotating cylinders ($\omega_i, \omega_o \neq 0$), Singh, Ghosh & Alam (2022) explored the pattern transition scenario in the counter-rotation regime ($\Omega < 0$) of suspension TCF. They found that while the overall transition sequence remains the same for $\Omega \geq -0.25$ as in the case of the purely inner cylinder rotation ($\Omega = 0$), a novel transition occurs at $\Omega = -0.5$ in which the stationary TVF bifurcates directly into a quasi-periodic state (characterized by two incommensurate frequencies), called the modulated wavy vortex (MWV), even for a pure fluid ($\phi = 0$). They also carried out a detailed analysis of the transition scenario for the exact counter-rotation case ($\Omega = -1$) where the CCF bifurcates into a non-axisymmetric state (SVF) that further transitions to a quasi-periodic state (nonlinear ISV), followed by a chaotic state, called the non-propagating interpenetrating spirals (NISs). The follow-up article of Alam & Ghosh (2023) came out with a master scaling relation for the dimensionless torque that holds over large ranges of the Taylor number and the counter-rotation ratio, encompassing primary, secondary and tertiary states. An overview of all works on suspension TCF can be found in the review article of Baroudi *et al.* (2023). The present experiments aim to uncover the pattern transition route in the 'co-rotation' regime ($\Omega > 0$) of suspension TCF, with the goal to understand the effects of particle loading and co-rotation on the emerging pattern dynamics.

## 2. Experimental details

All experiments are carried out in a Taylor–Couette (TC) cell mounted on a Twin-Drive MCR-702 rheometer (Anton Paar GmbH, Austria) that has been used in our previous studies (Singh *et al.* 2022; Alam & Ghosh 2023). Two independently rotating motors are used to drive the inner and outer cylinders by specifying the rotation ratio $\Omega = \omega_o/\omega_i = f_o/f_i$ in the 'co-rotation' regime ($\Omega > 0$). Thanks to the beta-version of the 'RheoCompass' software (2022, private communication with Anton-Paar R&D team, Graz, Austria), we could explore the co-rotation regime of the TCF, while the original software was written for $\Omega < 0$; this also allowed us to sweep up to a maximum frequency of 50 Hz, increasing the range of Reynolds numbers by a factor of 2.5 in comparison to our recent work in the counter-rotation regime (Singh *et al.* 2022; Alam & Ghosh 2023). The aspect ratio of the TC cell is $\Gamma = h/\delta = h/(r_o - r_i) \approx 8.46$ and the radius ratio is $\eta = r_i/r_o \approx 0.891$, with $(h, r_i, r_o) = (16.5, 16.0, 17.95)$ mm. The suspension is made of rigid PMMA microspheres of mean diameter $d \approx 50\,\mu$m and material density of $\rho \approx 1190\,\mathrm{kg\,m^{-3}}$ and a density-matched solvent which is a ternary mixture of water, glycerine and ammonium thiocyanate, and we refer readers to the above two papers for other details on experiments.

For given $(\Omega,\ \phi)$, the experiments are started from $f = f_{min} \sim 0$ and stopped at $f = f_{max} = \max\{f_i, f_o\} = 50$ Hz by increasing the rotation frequency at a slow ramping rate – such ramp-up protocols are referred to as 'up-sweep' runs. However, for experiments which consist of both up- and down-sweep runs, after completing the up-sweep run, the rotation frequency remains constant at $f = f_{max}$ for a sufficiently long time (600 s) beyond which a ramp-down protocol is followed by decreasing the rotation frequency from $f = f_{max}$ to $f_{min}$. We set the dimensionless ramping rate to $|dRe(\phi)/d\tau| = 0.05/\mu_r(\phi)$, where $Re(\phi) = \max\{Re_i(\phi), Re_o(\phi)\}$ with $Re_i(\phi) = \rho\omega_i r_i\delta/\mu(\phi)$ and $Re_o(\phi) = \rho\omega_o r_o\delta/\mu(\phi)$ being the inner and outer Reynolds numbers, respectively, and $\tau = t/\tau_{vis}$, with $\tau_{vis} = \rho\delta^2/\mu(\phi)$ being the viscous diffusion time; $\mu(\phi) = \mu(0)(1 - \phi/\phi_m)^{-2}$ is the suspension viscosity, $\mu(0) \approx 7.90$ mPa s is the shear viscosity of the solvent, both measured at T = 22 °C, $\phi_m = 0.585$ is the maximum packing fraction (at random loose packing), and $\mu_r(\phi) = \mu(\phi)/\mu(0) \geq 1$ is the relative viscosity of suspension (Guazzelli & Pouliquen 2018). During up-sweep and down-sweep runs, the rotation frequency is increased and decreased in steps by staying for 10 s ($\sim 70\tau_{vis}$ at $\phi = 0.3$) at each step. Note that the maximum particle Reynolds number is estimated as $Re_p(\Omega) = \rho\dot{\gamma}_{app}d_p^2/\mu(0) = Re_i^{\max}|1 - \Omega/\eta|(d/\delta)^2 = (0.90, 0.26)$ at $\Omega = (0.05, 0.65)$, with $\dot{\gamma}_{app} = |\omega_i r_i - \omega_o r_o|/\delta$ being the apparent shear rate across the annular gap (Alam & Ghosh 2023). The corresponding particle Stokes number and Péclet number are estimated as $St_p = m_p\dot{\gamma}_{app}/3\pi\mu(0)d_p = (0.05, 0.014)$ and $Pe = 3\pi\mu(0)d_p^3\dot{\gamma}_{app}/4k_BT = O(10^9, 10^8)$, respectively, at $\Omega = (0.05, 0.65)$. Therefore, the particles can be treated as non-Brownian particles for which the inertial effects, $Re_p = O(1)$, are non-negligible. All experiments are performed in an air-conditioned room at T = 22 ± 0.5 °C.

For flow visualizations, a small amount (<0.1 %, Ramesh *et al.* 2019; Singh *et al.* 2022) of anisotropic mica flakes is added to the suspension, and three 41 W LED panels are used to illuminate the TC cell. The video images of surface flow patterns are continuously captured using a Nikon (D750 DSLR) camera at a frame rate of $60\,\mathrm{s^{-1}}$. In addition, a high-speed camera, Phantom v9 (DANTEC DYNAMICS), is used to capture images at regular intervals at a frame rate of $200\,\mathrm{s^{-1}}$ so as to capture high-frequency modes. The captured images are then analysed to extract information on the flow states by constructing space–time diagrams and frequency maps.

## 3. Results and discussion

Experiments have been conducted by choosing a value of $\Omega = (0.05, 0.1, 0.2, 0.3, 0.5, 0.65)$ in the co-rotation regime for different particle volume fractions $\phi = (0, 0.05, 0.1, 0.15, 0.2, 0.3)$; the case of pure inner cylinder rotation is approximated by conducting experiments at $\Omega = -10^{-3} \approx 0$ (Singh *et al.* 2022). The maximum explored value of $\Omega = 0.65$ is close to the Rayleigh stability line (Rayleigh 1917) of $\Omega = \eta^2 \approx 0.794$ beyond which the TCF is known to be stable. We have carried out a set of experiments at a rotation ratio of $\Omega = \omega_o/\omega_i = 0.82 > \eta^2$ for $\phi = (0, 0.15)$ and found that the flow remains stable over a range of shear Reynolds number $Re_s \leq Re_s^{max}(\phi)$, see (3.1). Note that the present value of $Re_s^{max}(\phi)$ for a specified $\phi$ is set by the maximum frequency $f_{max} = 50$ Hz of the two motors, and $Re_s^{max}(\phi)$ decreases with increasing $\Omega$ and approaches zero in the limit of the solid-body rotation ($\Omega \to 1$, i.e. $\omega_i = \omega_o$), see the lower boundary of the hatched region in figure 1. We first discuss how the co-rotation ratio ($\Omega > 0$) affects the transition scenario at fixed values of $\phi$ in § 3.1, followed by results in § 3.2 for the effect of particle loading on patterns at fixed $\Omega$ and discussions and theoretical perspectives in § 3.3.

### 3.1. *Effect of co-rotation on pattern transitions*

Figure 1(*a–c*) displays the phase diagrams of patterns in the $(\Omega, Re_s(\phi))$-plane for $\phi = 0$, 0.15 and 0.3, respectively, where

$$Re_s(\Omega, \phi) = \frac{2}{1+\eta}|\eta Re_o(\phi) - Re_i(\phi)| = \frac{2Re_i(\phi)}{1+\eta}|1-\Omega| \tag{3.1}$$

is the shear Reynolds number (Dubrulle *et al.* 2005; Eckhardt, Grossmann & Lohse 2007; Singh *et al.* 2022). In each panel, the empty and filled symbols mark the critical values of $Re_s(\Omega, \phi)$ during up- and down-sweep runs, respectively, at which the bifurcations/transitions between two states occur. The lower boundary of the black hatched region in each panel denotes the maximum range of $Re_s(\phi)$ explored (with $f_{max} = 50$ Hz) at given $(\Omega, \phi)$, while the grey patches (such as in the inset of figure 1*b*) represent the hysteresis regions.

#### 3.1.1. *TCF of particle-free ($\phi = 0$) Newtonian fluid under co-rotation*

For the particle-free Newtonian fluid ($\phi = 0$), it is seen from figure 1(*a*) that the primary bifurcating state from the laminar circular Couette flow (CCF) is a stationary axisymmetric state, called the TVF, for all $\Omega$. The image analyses helped to correctly identify the critical shear Reynolds number $Re_s^{c1}(\phi)$ at the CCF $\leftrightarrow$ TVF transition. Figure 1(*a*) reveals that $Re_s^{c1}(\phi)$ gradually decreases with increasing $\Omega$, implying the destabilization role of co-rotation at the onset of the primary instability (Taylor 1923; Coles 1965; Andereck *et al.* 1986). For a quantitative comparison, the present experimental data on $Re_s^{c1}(\Omega, \phi = 0)$ are compared with the marginal stability curve of Esser & Grossmann (1996),

$$\frac{r_n^2 - r_p^2}{r_p^2}\left(\frac{r_i\alpha\sqrt{Re_s}}{r_n\sqrt{\eta}}\right)^4 = \Psi\left(a\frac{\delta_n}{\delta}\right)^{-4}, \tag{3.2}$$

where $\delta = r_o - r_i$ is the gap width, $r_n = r_i\sqrt{(\Omega-1)/(\Omega-\eta^2)}$ is the neutral radius, $\delta_n = r_n - r_i$, $r_p = r_i + (\delta/2)\Psi(a\delta_n/\delta)$, $a = (1-\eta)[\sqrt{(1+\eta)^3/2(1+3\eta)} - \eta]^{-1}$, $\alpha = 0.1566$, and $\Psi(x) = x$ and 1, respectively, for $x < 1$ and $x \geq 1$. Equation (3.2) is denoted

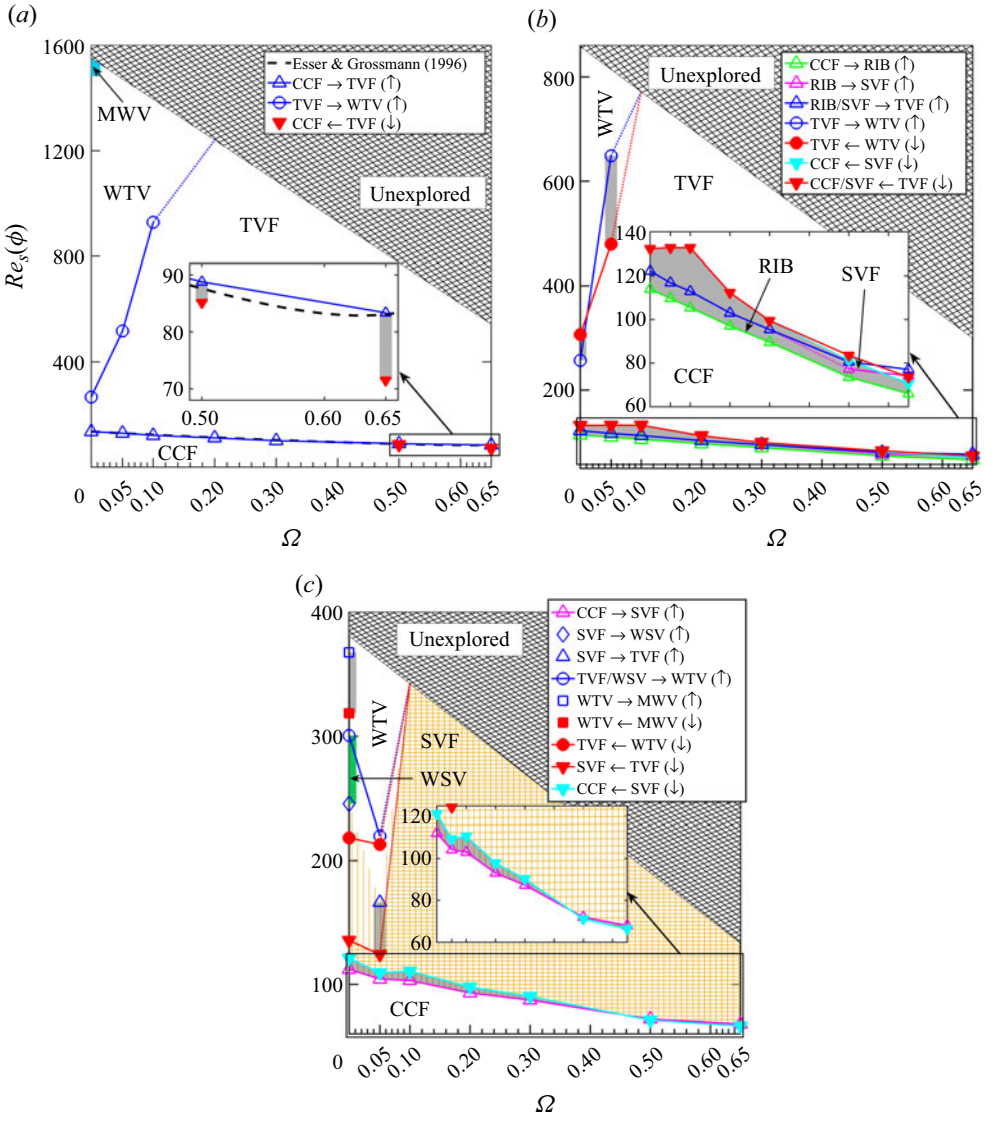


Figure 1. Phase diagrams of patterns in the $(\Omega, Re_s(\phi, \Omega))$-plane at (*a*) $\phi = 0$, (*b*) $\phi = 0.15$ and (*c*) $\phi = 0.3$. The empty and filled symbols (with and without lines), respectively, represent the onset values of $Re_s(\phi)$ at bifurcations during up- and down-sweep runs; the grey patches in each panel denote the hysteresis regions. The zoomed view of the selected region in each figure is shown in the corresponding inset. The dashed line in panel (*a*) represents the marginal stability curve (3.2) of Esser & Grossmann (1996). The yellow hatched regions in panel (*c*) mark the parameter space where the SVF is observed during up-sweep (vertical lines) and down-sweep (horizontal lines) runs.

by the black dashed curve in figure 1(*a*) which agrees well with our up-sweep data (open triangles) on $Re_s^{c1}(\Omega)$. From a comparison between the up- and down-sweep data at $\Omega = 0.5$ and 0.65 in the inset of figure 1(*a*), we find that the primary bifurcation is hysteretic at large enough $\Omega$ and the degree of hysteresis (i.e. the height of the grey patches in the inset, $\Delta Re_s$) is larger at $\Omega = 0.65$ compared with at $\Omega = 0.5$. Although the CCF $\leftrightarrow$ TVF transition is known to be non-hysteretic at $\Omega \geq 0$ in the case of large-$\Gamma$

TC cells (Taylor 1923; Coles 1965; Hegseth, Baxter & Andereck 1996), the presence of axial constraints in a small-$\Gamma$ cell can make the primary transition hysteretic as reported by Heise *et al.* (2013) and confirmed in the present study ($\Gamma \approx 8.46$).

Beyond the primary bifurcation at $Re_s > Re_s^{c1}$, the TVF undergoes a secondary bifurcation at $Re_s = Re_s^{c2}$ that gives birth to an oscillatory state, called the WTV, marked by empty blue circles in figure 1(*a*). It is evident from figure 1(*a*) that $Re_s^{c2}(\Omega)$ increases rapidly with increasing co-rotation, and the stabilizing role of the co-rotation at the secondary onset agrees qualitatively with previous experiments (Coles 1965; Andereck *et al.* 1986). Note in figure 1(*a*) that the WTV state disappears for $\Omega \geq 0.2$ over the range of $Re_s$ explored in the present study. Referring to the case where only the inner cylinder is rotating ($\Omega = -10^{-3} \approx 0$), we find that with further increase in $Re_s > Re_s^{c2}$, the WTV undergoes a tertiary bifurcation, leading to the modulated wavy vortex (MWV; the cyan region near the left top corner in figure 1*a*) at $Re_s(\Omega, \phi = 0) \geq Re_s^{c3}$; the latter is a quasi-periodic state, characterized by two incommensurate frequencies in the power spectrum of the scattered light intensity (Andereck *et al.* 1986; Singh *et al.* 2022). Note that the MWV is found over a small range of $Re_s(\phi)$ at $\Omega = -10^{-3}$ and ceases to exist at $\Omega \geq 0.05$ over the maximum range of $Re_s(\Omega, \phi)$ explored.

One notable difference of the present results with Andereck *et al.* (1986) is that the secondary and tertiary transitions to WTV and MWV occur at higher values of $Re_s^{c2}$ and $Re_s^{c3}$, respectively. This may be attributed to the smaller aspect ratio of our TC cell for which the Ekman vortices are likely to be stronger, thus delaying the onset of oscillatory motion (Cole 1976; Mullin & Benjamin 1980).

### 3.1.2. *Suspension TCF under co-rotation*

Moving on to suspensions, figure 1(*b*) displays the phase diagram of patterns at $\phi = 0.15$. The inset of figure 1(*b*) confirms (as by Majji *et al.*'s (2018) original work for the case of $\Omega = 0$) that the RIB, a 'non-axisymmetric' state, is the primary bifurcating state over $\Omega \in (0, 0.65)$ during the up-sweep run (marked by the green up-triangles), while during the down-sweep run, the TVF (marked by the filled red down-triangles) and the spiral vortex flow (SVF, marked by filled cyan down-triangles) are found as the primary bifurcating states over $\Omega = (0, 0.3)$ and $\Omega > 0.3$, respectively. Note that RIB exists over a small range of $Re_s(\phi)$ during the up-sweep run; it transitions to TVF with increasing $Re_s$ at $\Omega \leq 0.3$, and to SVF at $\Omega \geq 0.5$, with the latter finally transitioning to TVF with further increase in $Re_s$. Looking at the hysteretic/bistable (i.e. the coexistence of TVF and RIB/SVF) region, marked by the grey patch in the inset of figure 1(*b*), we find that the degree of hysteresis $\Delta Re_s^{c1}(\phi) = |Re_s^{c1}(\phi)_{\uparrow} - Re_s^{c1}(\phi)_{\downarrow}|$ decreases with increasing co-rotation.

The characteristic features of the RIB and SVF states can be ascertained from figures 2(*a*,*c*) and 2(*b*,*d*), respectively. While the SVF represents a helical wave that propagates along both axial and azimuthal directions, the RIB is a superposition of left- and right-handed spirals (Chossat & Iooss 1994), resulting in an axially standing wave that rotates along the azimuthal direction (Majji *et al.* 2018; Singh *et al.* 2022); the latter may also be called the rotating standing wave, RSW↔RIB. The space–time diagram of the RIB state in figure 2(*a*) resembles a checkerboard-like pattern, with a dominant frequency of $\omega_{RIB}/\omega_i \approx 0.1$, as marked by the green circle in figure 2(*c*). However, the dominant frequency of the SVF mode in figure 2(*d*) is located at $\omega_{SVF}/\omega_i \approx 0.72$, which is much larger than that of the RIB mode. This order-of-magnitude difference between the dominant frequencies at the onset of the SVF and RIB modes persists at all $\Omega$, see figure 3(*a*). The latter figure also confirms a key difference between SVF and RIB:

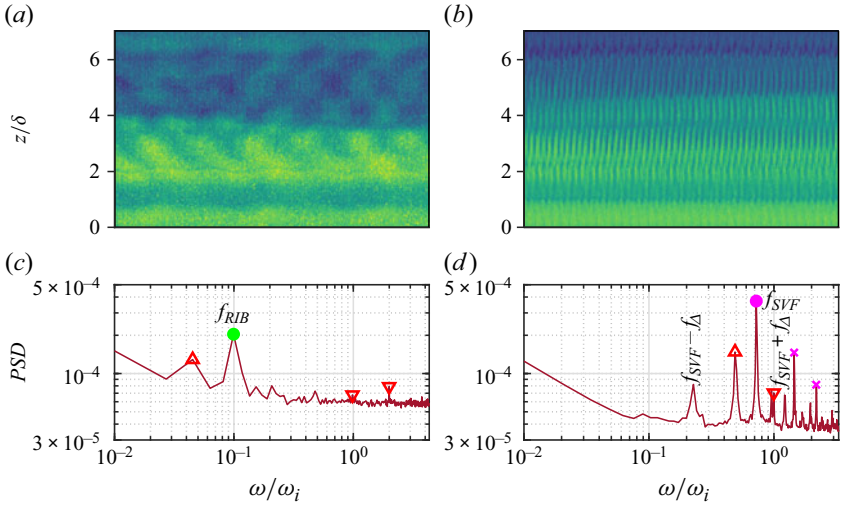


Figure 2. (*a*,*b*) Space–time diagrams over 8 s of the (*a*) ribbon (RIB) and (*b*) spiral vortex flow (SVF) states, and (*c*,*d*) the power spectra of the scattered light intensity as computed from images captured at a frame rate of $60\,\mathrm{s}^{-1}$. While the green circle in panel (*c*) refers to the frequency of RIB ($f_{RIB}$), the magenta circle and crosses in panel (*d*) represent frequency of the SVF mode ($f_{SVF}$) and its harmonics. The red down- and up-triangles mark the frequencies of the inner ($f_\nabla$) and outer ($f_\Delta$) cylinders, respectively, and their harmonics. Parameter values are (*a*,*c*) RIB at $(Re_s, \Omega, \phi) = (113.70, 0.05, 0.15)$ and (*b*,*d*) SVF at $(Re_s, \Omega, \phi) = (78.53, 0.5, 0.15)$ during up-sweep runs.

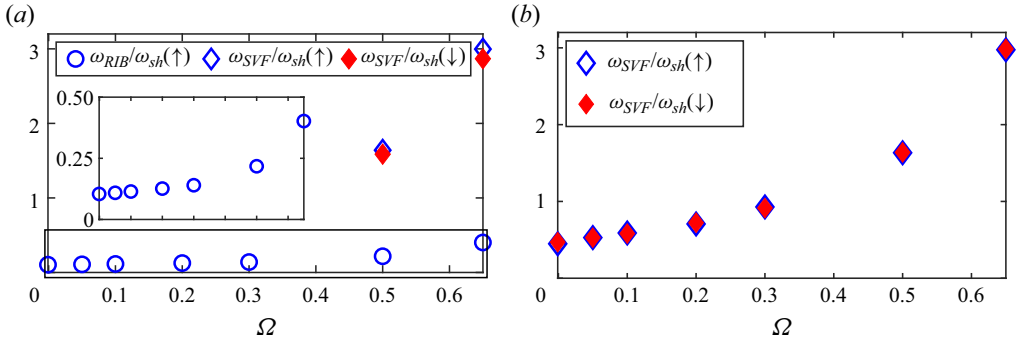


Figure 3. Dominant frequencies at the onset of RIB (circles) and SVF (diamonds), normalized by the effective rotation rate $\omega_{sh} = |\omega_i - \omega_o/\eta| = \omega_i|1 - \Omega/\eta|$, at (*a*) $\phi = 0.15$ and (*b*) $\phi = 0.3$. The empty and filled markers, respectively, denote the SVF data (i.e. the FFT analyses of the images from the high-speed camera at 200 fps) for up- and down-sweep runs.

the frequency (normalized by the effective rotation rate $\omega_{sh} = \omega_i|1 - \Omega/\eta|$) of RIB is small and increases weakly with increasing co-rotation $\Omega$ (see the inset of figure 3*a*); however, the normalized frequency of the spiral vortices (at the onset) increases sharply with increasing $\Omega$ (marked by the diamond symbols in figure 3*a*).

With increasing $Re_s(\phi)$ in figure 1(*b*), the TVF bifurcates into WTV (marked by the blue circles) which is a tertiary state during the up-sweep run at $\Omega \leq 0.05$, with an overall bifurcation sequence of CCF→RIB→TVF→WTV. However, the WTV is found to be the secondary state due to the non-existence of RIB, i.e. WTV→TVF→CCF, during the down-sweep run, with the TVF↔WTV transition being hysteretic as marked by the

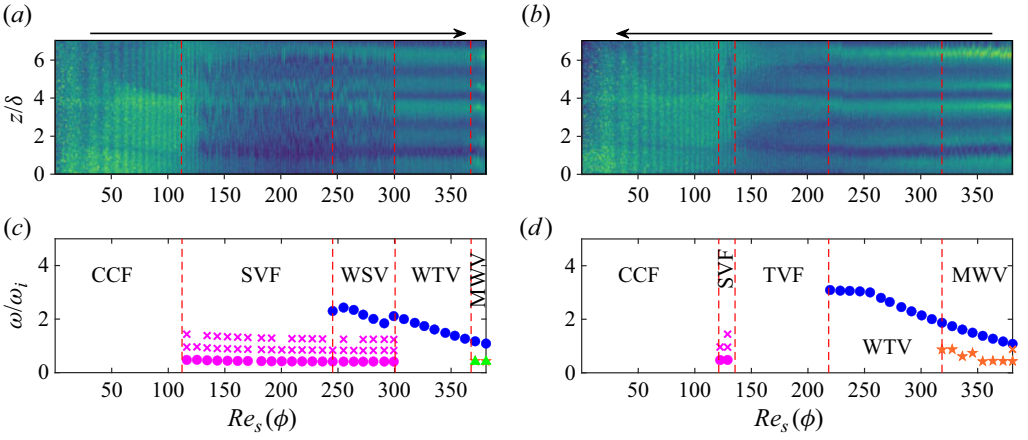


Figure 4. (*a*,*b*) Space–$Re_s(\phi)$ diagrams (from the DSLR camera at 60 fps) and (*c*,*d*) the normalized frequency $\omega/\omega_i$ versus $Re_s(\phi)$ (data from the high-speed camera at 200 fps), during (*a*,*c*) up-sweep and (*b*,*d*) down-sweep runs for $\phi = 0.3$ at $\Omega = -10^{-3}$.

vertical grey patch at $\Omega = 0.05$ in figure 1(*b*). Comparing figure 1(*b*) with its particle-free counterpart in figure 1(*a*), we find that the region of WTV in the ($Re_s$, $\Omega$)-plane shrinks with increasing $\phi$, indicating the stabilizing role of particles on the onset of oscillatory wavy vortices at $\Omega \geq 0$.

The pattern transitions differ significantly at higher particle loadings, see figure 1(*c*) which depicts the phase diagram of patterns in the ($\Omega$, $Re_s$)-plane at $\phi = 0.3$, with a major finding that the SVF is the primary bifurcating state at all $\Omega \in (0, 0.65)$ during both up- and down-sweep runs; the corresponding variation of the dominant frequency of the SVF mode at its onset with $\Omega$ can be ascertained from figure 3(*b*). It is seen in figure 1(*c*) that the effect of co-rotation on spiral vortices is to decrease the onset value of $Re_s^{c1}(\phi, \Omega)$ with increasing $\Omega$; the rate of decrease of $Re_s^{c1}$ with $\Omega$ (i.e. $dRe_s^{c1}/d\Omega$) is larger at $\phi = 0.3$ than that at $\phi = 0.15$, indicating that the co-rotation has more destabilizing effect on primary bifurcation at higher particle loading. The grey patch in the inset of figure 1(*c*) clarifies that there is a small hysteresis for the CCF↔SVF transition at $\Omega \leq 0.3$, but the degree of hysteresis ($\Delta Re_s(\phi)$) decreases with increasing $\Omega$, eventually becoming non-hysteretic at $\Omega \geq 0.5$. The phase diagram in figure 1(*c*) can be sub-divided into two parts: (i) $\Omega \geq 0.1$ over which only the SVF is found in the explored range of $Re_s(\phi)$; and (ii) $\Omega \leq 0.05$ over which the SVF undergoes successive transitions to produce secondary and higher-order states. The sequence of latter transitions can be appreciated from figure 4 that depicts (*a*,*b*) the space-$Re_s(\phi)$ diagrams and (*c*,*d*) the normalized frequency maps $\omega/\omega_i$ at $\Omega = -10^{-3} \approx 0$.

For the 'up-sweep' run in figure 4(*a*,*c*) at $\phi = 0.3$, the SVF state (denoted by the filled magenta circles in panel *c*) exists at $112.2 \leq Re_s(\phi) < 245.3$; the magenta crosses represent the harmonics of the SVF mode. A high-frequency wavy mode, marked by the filled blue circles in figure 4(*c*), appears in the frequency map at $Re_s(\phi) \geq 245.3$. Interestingly, both the spiral mode and the wavy mode are found to coexist at $245.3 \leq Re_s(\phi) < 300.5$ over which the pattern resembles wavy spiral vortices (WSV). A snapshot of the WSV state is shown in figure 5(*a*) that clarifies the waviness of the spiral vortices, while figure 5(*c*) reveals the presence of two distinct frequencies ($f_{SVF}$ and $f_w$) marked by magenta and blue circles, respectively. The WSV mode ceases to exist at $Re_s(\phi) \geq 300.5$, and the WTV state takes over at $300.5 \leq Re_s(\phi) < 367.7$, see figure 4(*c*). The structural

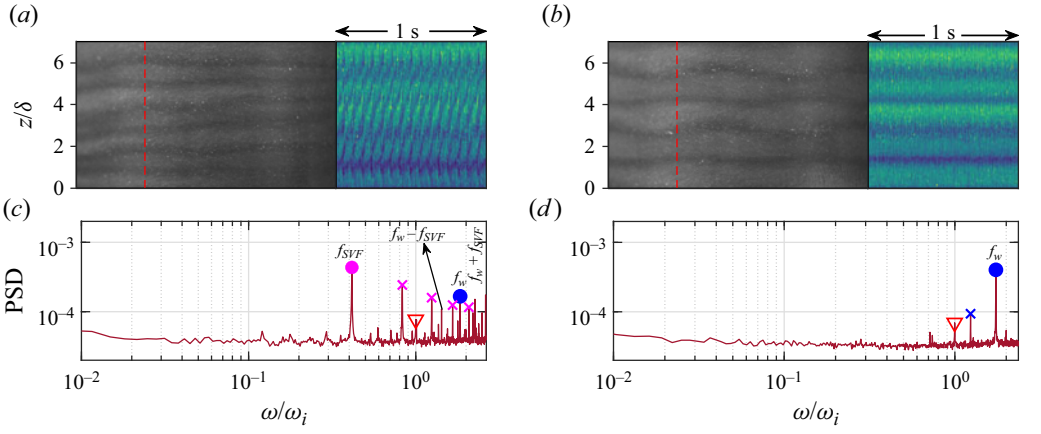


Figure 5. Patterns of (*a*,*c*) WSV (wavy spiral vortex) at $Re_s(\phi) = 290.90$ and (*b*,*d*) WTV (wavy Taylor vortex) at $Re_s(\phi) = 326.30$ during up-sweep run at $\Omega = -10^{-3}$ for $\phi = 0.3$, consisting of (*a*,*b*) snapshots and space–time plots and (*c*,*d*) power spectra.

characteristics of the single-frequency WTV mode can be ascertained from figure 5(*b*) and the corresponding power spectrum in figure 5(*d*) at $Re_s(\phi) = 326.3$. At $Re_s(\phi) \geq 367.7$, we find the appearance of an additional low-frequency mode (incommensurate) in figure 4(*c*), a distinct characteristic of a quasi-periodic mode, called the MWV.

The above MWV state bifurcates into WTV at $Re_s(\phi) \approx 318.5$, during the 'down-sweep' run (figure 4*b*,*d*) with decreasing $Re_s(\phi)$, which continues to exist until $Re_s(\phi) \approx 218.3$; the WTV bifurcates into TVF at $Re_s(\phi) \approx 218.3$ that further transitions to SVF and finally the laminar CCF state appears at $Re_s(\phi) \leq 121.2$. Increasing the co-rotation ratio slightly to $\Omega = 0.05$ (see figure 1*c*), the WSV and MWV states disappear and a transition sequence of CCF $\leftrightarrow$ SVF $\leftrightarrow$ TVF $\leftrightarrow$ WTV is found during both up- and down-sweep runs, with the primary bifurcation representing a non-axisymmetric (SVF) mode.

### 3.2. *Effect of particle loading at fixed Ω and the scaling of SVF frequencies*

Figures 6(*a*) and 6(*b*) display the phase diagrams of patterns in the $(\phi, Re_s(\phi, \Omega))$ plane at $\Omega = 0.05$ and 0.65, respectively, that refer to of (*a*) a nearly stationary outer cylinder ($\Omega = 0.05 \sim 0$) and (*b*) close to the Rayleigh line $\Omega = \eta^2 \approx 0.8$ (Rayleigh 1917). The inset of figure 6(*a*) indicates that the TVF, RIB and SVF appear as the primary bifurcating state at $\phi \leq 0.05$, $0.1 \leq \phi \leq 0.2$ and $\phi > 0.2$, respectively. Note also in figure 6(*a*) that while a transition sequence of CCF $\leftrightarrow$ SVF $\leftrightarrow$ TVF $\leftrightarrow$ WTV holds at $\phi = 0.3$ during both up- and down-sweep runs, the SVF emerges as an intermediate state between RIB and TVF during the up-sweep run at $\phi = 0.2$. An overall transition sequence of CCF$\rightarrow$RIB$\rightarrow$TVF$\rightarrow$WTV is found during the up-sweep run at $\phi = (0.1, 0.15)$, but the RIB state disappears during the down-sweep run at $\phi = 0.15$, see the inset of figure 6(*a*). For the higher co-rotation case of $\Omega = 0.65$ in figure 6(*b*), the $(\phi, Re_s(\phi))$-plane can be divided into two regions where the primary bifurcating states are axisymmetric (TVF at $\phi < 0.15$) and non-axisymmetric (SVF/RIB at $\phi \geq 0.15$) modes, depending on the particle loading. The higher-order mode transitions are absent in figure 6(*b*), due to the smaller range of explored $Re_s$ (with $f_{max} = 50$ Hz) at $\Omega = 0.65$.

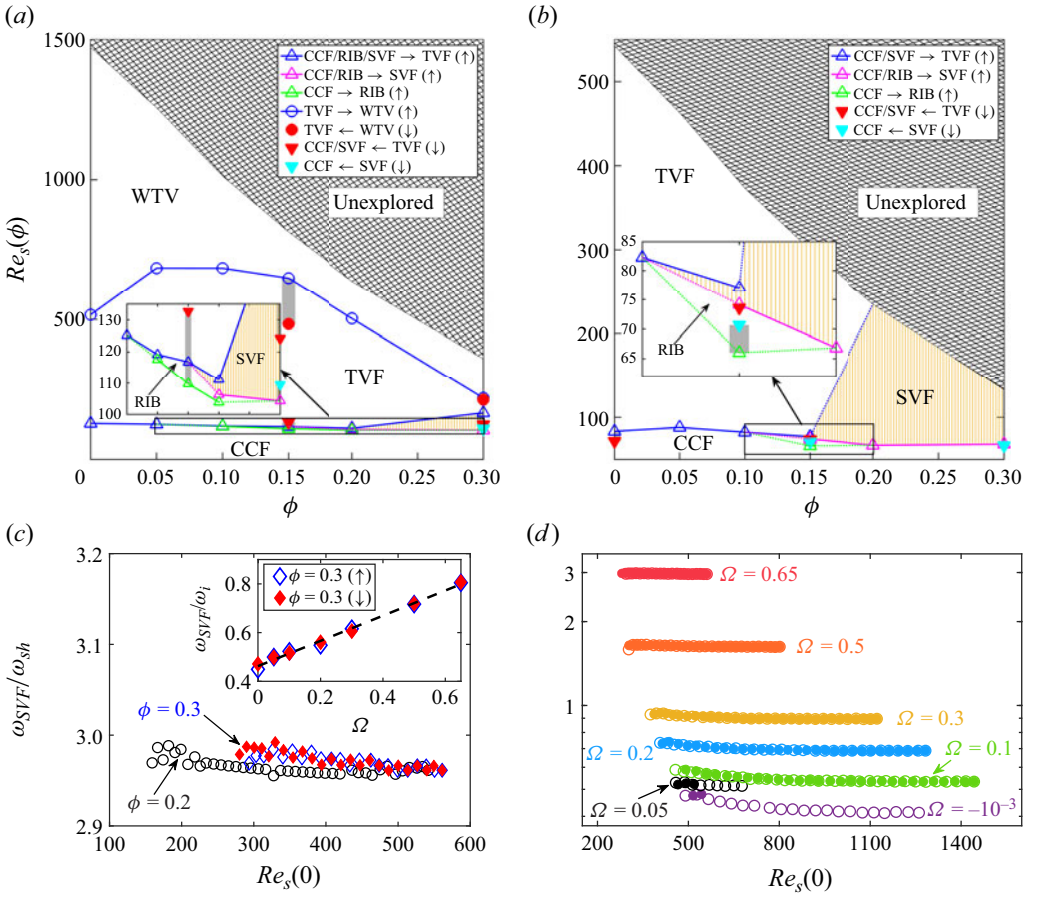


Figure 6. (*a*,*b*) Phase diagram of patterns at (*a*) $\Omega = 0.05$ and (*b*) $\Omega = 0.65$; the line style and colour coding are the same as in figure 1. Enlarged views of selected regions in panels (*a*,*b*) are shown in corresponding insets. (*c*) Variations of the normalized frequency of the spiral vortices, $\omega_{SVF}/\omega_{sh}$, with (i) $Re_s(0)$ at $\Omega = 0.65$ for different $\phi$ (main panel) and (ii) $\omega_{SVF}/\omega_i$ versus $\Omega$ at $\phi = 0.3$ (inset); the dashed line in the inset of panel (*c*) is given by (3.3). (*d*) '$Re_s(0)$-independent' frequency of spirals at $\phi = 0.3$ for different $\Omega$; the open and filled symbols for each $\Omega$ denote the data for up- and down-sweep runs, respectively.

Collectively, figure 6(*a*,*b*) indicates that the effect of particle loading at $\Omega = 0.05$ and 0.65 is to decrease the critical values of $Re_s^{c1}(\phi)$ for primary bifurcations, confirming the destabilizing role of particles on the onset of primary states (TVF/SVF/RIB). However, the critical Reynolds number $Re_{TVF}^{WTV}(\phi)$ for the TVF↔WTV transition at $\Omega = 0.05$ (figure 6*a*) has a non-monotonic dependence on the particle loading, indicating the dual role of stabilization (at $\phi < 0.10$) and destabilization (at $\phi \geq 0.10$) on the WTV mode.

The SVF such as in figures 1(*c*) and 6(*a*,*b*) truly represent particle-induced patterns since they are absent in the particle-free TCF. Two distinctive features of these spirals are as follows: its wave speed (i) is nearly independent of the 'fluid' shear Reynolds number $Re_s(0)$; and (ii) increases weakly with increasing particle volume fraction ($\phi$), as confirmed in the main panel of figure 6(*c*) at $\Omega = 0.65$. This finding is in stark contrast to the scaling for the wave speed of the 'fluid-induced' spirals, $\omega_{SVF} \propto Re_s(0)^{-0.78}\mu_r(\phi)^{0.42}$ (Singh *et al.* 2022), that are found in the counter-rotation regime of the suspension TCF. The third distinctive feature of the 'particle-induced' spirals is that its wave speed increases

with increasing $\Omega$,

$$\frac{\omega_{SVF}(\Omega)}{\omega_i} = \alpha_1\Omega + \alpha_2 \quad \Rightarrow \quad \frac{\omega_{SVF}(\Omega)}{\omega_{sh}} = (\alpha_1\Omega + \alpha_2)\left(1 - \frac{\Omega}{\eta}\right)^{-1}, \tag{3.3}$$

see the black dashed line in the inset of figure 6(*c*), indicating the linear variation of $\omega_{SVF}/\omega_i$ with the rotation ratio $\Omega$; here, $(\alpha_1, \alpha_2) \approx (0.522, 0.46)$ and $\omega_{sh} = \omega_i(1 - \Omega/\eta)$ is the effective rotation rate across the annular gap. The limiting value of $\omega_{SVF}(\Omega = 0) \approx 0.46\omega_i$ from (3.3) agrees closely with that reported by Ramesh *et al.* (2019), $\omega_{SVF}/\omega_i \approx 0.45$, see their figure 16(*c*), for the case of the pure inner cylinder rotation ($\Omega = 0$). While the data in the inset of figure 6(*c*) represent the onset SVF frequency, its independence with $Re_s(0)$ at any $\Omega$ is confirmed in figure 6(*d*). We conclude that the spiral vortices become progressively faster as we move closer to the Rayleigh line ($\Omega = \eta^2$ or $Re_o = \eta Re_i$) beyond which the TCF is stable and the fluid inertia $Re_s(0)$ has a negligible effect on its wave speed.

### 3.3. *Discussion and theoretical perspectives*

Returning to figure 4, the observed differences in the transition sequence for $\phi = 0.3$ between up- (figure 4*a*,*c*) and down-sweep (figure 4*b*,*d*) runs indicate the multi-stability among different patterns at $\Omega = -10^{-3} \approx 0$ for which the transitions occur with pronounced hysteresis. Such hysteretic patterns/states mirror previous findings at $\Omega = 0$ (Majji *et al.* 2018; Ramesh *et al.* 2019; Dash *et al.* 2020; Moazzen *et al.* 2022) and are known to persist in the counter-rotation regime $\Omega < 0$ (Singh *et al.* 2022) too. Concerning the effect of co-rotation on hysteresis, the insets of figure 1(*b*,*c*) confirmed that the degree of primary hysteresis decreases in the co-rotation regime for finite $\phi > 0$.

One interesting finding in figure 4(*c*,*d*) is that the fundamental (passage) frequency of the wavy vortices $\omega_{WTV}/\omega_i$ decreases with increasing shear Reynolds number $Re_s(\phi)$ at $\Omega \approx 0$; we verified that this observation holds for all $\Omega > 0$ and $\phi$. This result echoes the previous findings of: (i) Singh *et al.* (2022) in the counter-rotating ($\Omega < 0$) suspension TCF and (ii) King *et al.* (1984) in the particle-free TCF at $\Omega = 0$. Possible reasons for the initial decay of $\omega_{WTV}(Re_s)$ with increasing $Re_s$ could be: (i) the increase in the wave-length of the wavy vortices; (ii) the generation of the harmonics of the fundamental mode; and (iii) the appearance of incommensurate modes (MWV) in the same limit – this remains an open issue for the future.

The future work on theoretical fronts should focus on predicting the onset of primary and higher-order transitions from linear (Taylor 1923; Majji *et al.* 2018; Gillissen & Wilson 2019) and nonlinear (Shukla & Alam 2009) stability analyses or direct numerical simulations (Kang & Mirbod 2021; Kang *et al.* 2024) of the pertinent continuum equations (Nott & Brady 1994; Morris & Boulay 1999). The underlying constitutive model for the particle stress must account for inertial migration phenomena (Majji & Morris 2018; Ramesh *et al.* 2019; Baroudi *et al.* 2020) since the particle Reynolds number $Re_p \sim O(1)$ remains an order-one quantity in all these experiments. The discrepancies between model predictions (Gillissen & Wilson 2019; Kang & Mirbod 2021) and experimental results (Majji *et al.* 2018; Ramesh *et al.* 2019) have been critically analysed in a recent review article by Baroudi *et al.* (2023) who concluded that the existing continuum models are not adequate to describe the behaviour of inertial suspensions. A stringent test of the applicability of such theoretical models would be to verify if they can predict the distinction between particle-induced and fluid-induced spirals in terms of their wave speeds (3.3), a key finding of the present work.

## 4. Conclusions

Based on the first set of experiments in the co-rotation regime ($\Omega \geq 0$) of the suspension Taylor–Couette flow (TCF), we showed that while the bifurcation sequence of CCF $\leftrightarrow$ TVF $\leftrightarrow$ WTV holds in a dilute suspension ($\phi \leq 0.05$), the non-axisymmetric states, such as the SVF and RIB, are born as primary bifurcations with increasing particle loading ($\phi \geq 0.1$), as summarized in figures 1(*b*,*c*) and 6(*a*,*b*). The latter states are analogues of the 'particle-induced' patterns reported in the recent studies at $\Omega = 0$ (Majji *et al.* 2018; Ramesh *et al.* 2019). Both the co-rotation ($\Omega$) and the particle loading ($\phi$) are found to promote an early onset of the primary instability (TVF/SVF/RIB) and hence destabilizing. Increasing $\Omega$ delayed/suppressed the onset of WTV, indicating its stabilizing role on the secondary/tertiary WTV state, but the particle loading can stabilize ($\phi < 0.1$) or destabilize ($\phi \geq 0.1$) WTV at small $\Omega \sim 0$. The distinguishing feature of the 'particle-induced' spiral vortices is quantified in terms of its wave speed which is found to increase with increasing $\Omega$ but remain nearly independent of the fluid inertia ($Re_s(0)$) – the latter finding is in contrast to the strong dependence on ($Re_s(0), \phi$) of the wave speed of the 'fluid-induced' spirals (Singh *et al.* 2022) that operate in the counter-rotating TCF (Coles 1965; Andereck *et al.* 1986). Theoretical explanations of the particle-induced signatures on our experimental results are awaited.

**Acknowledgements.** We sincerely thank Mr D. Das and Dr S. Raha of Anton-Paar India Pvt. Ltd. for arranging discussions with the R&D Team of Anton-Paar GmBH (Graz, Austria) – this led to the updated version (2022) of the RheoCompass software for the co-rotation regime of two motors. M.G. acknowledges the Science and Engineering Research Board (India) for the Postdoctoral Fellowship (PDF/2020/000916) during 2021–2022; he also acknowledges JNCASR for continued support (2023–) via the Centre's Postdoctoral Fellowship.

**Declaration of interests.** The authors report no conflict of interest.

**Author ORCIDs.**
Manojit Ghosh https://orcid.org/0000-0003-1439-1797;
Meheboob Alam https://orcid.org/0000-0002-8900-5224.

## References

Alam, M. & Ghosh, M. 2023 Unified torque scaling in counter-rotating suspension Taylor–Couette flow. *Phil. Trans. R. Soc.* A **381** (2243), 20220226.

Ali, M.E., Mitra, D., Schwille, J.A. & Lueptow, R.M. 2002 Hydrodynamic stability of a suspension in cylindrical Couette flow. *Phys. Fluids* **14** (3), 1236–1243.

Andereck, C.D., Liu, S.S. & Swinney, H.L. 1986 Flow regimes in a circular Couette system with independently rotating cylinders. *J. Fluid Mech.* **164**, 155–183.

Baroudi, L., Majji, M.V. & Morris, J.F. 2020 Effect of inertial migration of particles on flow transitions of a suspension Taylor–Couette flow. *Phys. Rev. Fluids* **5**, 114303.

Baroudi, L., Majji, M.V., Peluso, S. & Morris, J.F. 2023 Taylor–Couette flow of hard-sphere suspensions: overview of current understanding. *Phil. Trans. R. Soc.* A **381** (2243), 20220125.

Chossat, P. & Iooss, G. 1994 *The Couette-Taylor Problem*. Springer.

Cole, J.A. 1976 Taylor-vortex instability and annulus-length effects. *J. Fluid Mech.* **75**, 1–15.

Coles, D. 1965 Transition in circular Couette flow. *J. Fluid Mech.* **21**, 385–425.

Couette, M.M. 1888 Sur un nouvel appareil pour l'etude du frottement des fluids. *Comptes. Rend.* **107**, 388–390.

Dash, A., Anantharaman, A. & Poelma, C. 2020 Particle-laden Taylor–Couette flows: higher-order transitions and evidence for azimuthally localized wavy vortices. *J. Fluid Mech.* **903**, A20.

Dubrulle, B., Dauchot, O., Daviaud, F., Longaretti, P-Y, Richard, D. & Zahn, J-P. 2005 Stability and turbulent transport in Taylor–Couette flow from analysis of experimental data. *Phys. Fluids* **17** (9), 095103.

DUTCHER, C.S. & MULLER, S.J. 2009 Spatio-temporal mode dynamics and higher order transitions in high aspect ratio Newtonian Taylor–Couette flows. *J. Fluid Mech.* **641**, 85–113.

ECKHARDT, B., GROSSMANN, S. & LOHSE, D. 2007 Torque scaling in turbulent Taylor–Couette flow between independently rotating cylinders. *J. Fluid Mech.* **581**, 221–250.

ESSER, A. & GROSSMANN, S. 1996 Analytic expression for Taylor–Couette stability boundary. *Phys. Fluids* **8**, 1814–1819.

GILLISSEN, J.J.J. & WILSON, H.J. 2019 Taylor–Couette instability in sphere suspensions. *Phys. Rev. Fluids* **4**, 043301.

GOLLUB, J.P. & SWINNEY, H.L. 1975 Onset of turbulence in a rotating fluid. *Phys. Rev. Lett.* **35**, 927–930.

GROSSMANN, S., LOHSE, D. & SUN, C. 2016 High–Reynolds number Taylor–Couette turbulence. *Annu. Rev. Fluid Mech.* **48**, 53–80.

GUAZZELLI, E. & POULIQUEN, O. 2018 Rheology of dense granular suspensions. *J. Fluid Mech.* **852**, P1.

HEGSETH, J.J., BAXTER, G.W. & ANDERECK, C.D. 1996 Bifurcations from Taylor vortices between corotating concentric cylinders. *Phys. Rev.* E **53**, 507.

HEISE, M., HOFFMANN, C., WILL, C., ALTMEYER, S., ABSHAGEN, J. & PFISTER, G. 2013 Co-rotating Taylor–Couette flow enclosed by stationary disks. *J. Fluid Mech.* **716**, R4.

KANG, C. & MIRBOD, P. 2021 Flow instability and transitions in Taylor–Couette flow of a semidilute non-colloidal suspension. *J. Fluid Mech.* **916**, A12.

KANG, C., SCHATZ, M.F. & MIRBOD, P. 2024 Hysteresis and ribbons in Taylor–Couette flow of a semidilute noncolloidal suspension. *Phys. Rev. Fluids* **9**, 023901.

KING, G.P., LI, Y., LEE, W., SWINNEY, H.L. & MARCUS, P.S. 1984 Wave speeds in wavy Taylor-vortex flow. *J. Fluid Mech.* **141**, 365–390.

LUEPTOW, R.M., HOLLERBACH, R. & SERRE, E. 2023 Taylor–Couette and related flows on the centennial of Taylor's seminal *Philosophical Transactions* paper. *Phil. Trans. R. Soc.* A **381** (2243), 20220140.

MAJJI, M.V., BANERJEE, S. & MORRIS, J.F. 2018 Inertial flow transitions of a suspension in Taylor–Couette geometry. *J. Fluid Mech.* **835**, 936–969.

MAJJI, M.V. & MORRIS, J.F. 2018 Inertial migration of particles in Taylor–Couette flows. *Phys. Fluids* **30**, 033303.

MOAZZEN, M., LACASSAGNE, T., THOMY, V. & BAHRANI, S.A. 2022 Torque scaling at primary and secondary bifurcations in a Taylor–Couette flow of suspensions. *J. Fluid Mech.* **937**, A2.

MORRIS, J.F. & BOULAY, F. 1999 Curvilinear flow of non-colloidal suspensions: the role of normal stresses. *J. Rheol.* **43**, 1213–1237.

MULLIN, T. & BENJAMIN, T.B. 1980 Transition to oscillatory motion in the Taylor experiment. *Nature* **288**, 567–569.

NOTT, P.R. & BRADY, J.F. 1994 Pressure-driven flow of suspensions: simulation and theory. *J. Fluid Mech.* **275**, 157–199.

RAMESH, P. & ALAM, M. 2020 Interpenetrating spiral vortices and other coexisting states in suspension Taylor–Couette flow. *Phys. Rev. Fluids* **5**, 042301.

RAMESH, P., BHARADWAJ, S. & ALAM, M. 2019 Suspension Taylor–Couette flow: co-existence of stationary and travelling waves, and the characteristics of Taylor vortices and spirals. *J. Fluid Mech.* **870**, 901–940.

RAYLEIGH, LORD 1917 On the dynamics of revolving fluids. *Proc. R. Soc. Lond.* A **93**, 148–153.

SHUKLA, P. & ALAM, M. 2009 Landau-type order parameter equation for shear-banding in granular plane Couette flow. *Phys. Rev. Lett.* **103**, 068001.

SINGH, S.P., GHOSH, M. & ALAM, M. 2022 Counter-rotating suspension Taylor–Couette flow: pattern transition, flow multiplicity and the spectral evolution. *J. Fluid Mech.* **944**, A18.

SYNGE, S.L. 1938 On the stability of a viscous liquid between rotating co-axial cylinders. *Phil. Trans. R. Soc. Lond.* A **167**, 250–256.

TAYLOR, G.I. 1923 Stability of a viscous liquid contained between two rotating cylinders. *Phil. Trans. R. Soc.* A **223**, 289–343.